Next Nanotechnology 9 (2026) 100503

Contents lists available at ScienceDirect

Next Nanotechnology

journal homepage: www.sciencedirect.com/journal/next-nanotechnology

Research article

Tailoring the physicochemical and electrochemical properties of $Mg_{0.5+x}(Zr_{1-x}Al_x)_2(PO_4)_3$ ceramic electrolytes

M.S.A. Rani [a,b,*], M. Mustafa [c,d], F.M. Salleh [e], N.S. Mohamed [e], N.A. Mustaffa [f]

[a] Department of Physics, Faculty of Science, Universiti Putra Malaysia, UPM, Serdang, Selangor 43400, Malaysia
[b] Institute of Tropical Forestry and Forest Products (INTROP), Universiti Putra Malaysia, Serdang, Selangor 43400, Malaysia
[c] Institute of Advanced Studies, University of Malaya, Kuala Lumpur 50603, Malaysia
[d] Faculty of Industrial Sciences and Technology, Universiti Malaysia Pahang Al-Sultan Abdullah, Lebuh Persiaran Tun Khalil Yaakob, Kuantan, Pahang 26300, Malaysia
[e] Executive Director Office, Centre for Foundation Studies in Science, University of Malaya, Kuala Lumpur 50603, Malaysia
[f] Faculty of Applied Sciences, Universiti Teknologi MARA, Shah Alam, Selangor 40450, Malaysia

ARTICLE INFO

Keywords:
Ceramic electrolyte
Magnesium electrolyte
Nasicon structure
Al-doping

ABSTRACT

In this study, samples of Nasicon-type structured $Mg_{0.5+x}(Zr_{1-x}Al_x)_2(PO_4)_3$, ($0.0 \leq x \leq 0.4$) compound were synthesized via citrate assisted sol-gel method. The influences of structural modifications by partial substitution using trivalent ions (Al^{3+}) into the pristine $Mg_{0.5}Zr_2(PO_4)_3$ to the structural, particle size and electrical properties of the compounds were investigated. The crystal structure formation of $Mg_{0.5+x}(Zr_{1-x}Al_x)_2(PO_4)_3$ were affirmed using X-ray diffraction, while Rietveld refinement method was applied to clearly prove the formation of the structure. FESEM and particle size analysis confirmed that the particle size decreased with the increase of Al^{3+} compositions. The substitutions of Zr^{4+} with Al^{3+} in the pristine compound structure introduced extra-interstitial Mg^{2+} ions leading to enhanced conductivity. $Mg_{0.5+x}(Zr_{1-x}Al_x)_2(PO_4)_3$ compound with $x = 0.4$ exhibited the uttermost conductivity value of 7.33×10^{-5} S cm^{-1} at 773 K with the lowest activation energy of ~0.82 eV.

1. Introduction

The exploration of ionic conductivity in solids began in 1838, when Michael Faraday discovered that compounds like Ag_2S and PbF_2 exhibited appreciable ionic conduction. Over the following decades, many solid materials with significant ionic conductivity at elevated temperatures were identified. Notably, in the early 1960s, silver-ion conducting compounds such as $RbAg_4I_5$ were incorporated into electrochemical devices [1]. A major breakthrough occurred in 1976, when Goodenough and his colleagues introduced a new class of fast ion conductors known as NASICON (Na Super Ionic Conductor) [2]. The polyhedral skeleton consists of rigid (immobile) sub-arrays that can provide a large number of 3-dimensionally connected interstitial sites suitable for long range motion of monovalent cations. The structure consists of a three-dimensional framework of corner-shared ZrO_6 octahedra and PO_4 tetrahedra. This $[Zr_2(PO_4)_3]$ framework is highly stable because of its covalent nature and high melting points (>1650 °C). In the search of novel solid electrolytes for magnesium batteries, Nasicon-type compounds are interesting compound to be explored. The compounds have a structure that is large enough interstitial void to uptake guest species, large theoretical capacity, relatively high voltage and high structural stability based on a 3D framework [3,4].

There are limited research on the use of Mg^{2+} conducting compounds as electrolytes in magnesium batteries which can be explained by the divalent Mg-ion size difficult to diffuse in solid electrolytes, low specific energy of magnesium ion batteries compared to lithium counterparts and Mg-ion give narrow electrical window [5,6]. Makino and co-workers have reported about magnesium electrode using Nasicon-type compound [7,8]. They found that the substitution of Fe- and Cr- into parent $Mg_{0.5}Ti_2(PO_4)_3$ gave smaller unit cell volumes and higher theoretical capacity of 130–140 Ah kg^{-1}. In other works, Halim and co-researchers substituted Si^{2+} with Al^{3+} in $Mg_{0.5}Ti_2(PO_4)_3$ system resulting in an enhancement of conductivity due to the existence of Mg^{2+} interstitial ion in the compound [9]. Despite of these interesting properties of this group of compounds, a few disadvantages such as large lattice size of the structure needs to be solved by approaches such as modifying their unit cell dimension and ion concentration.

Various synthesis techniques have been employed to prepare ceramic electrolytes, including solid-state reaction, sol-gel, and combustion methods [10,11]. The solid-state method is simple and suitable

* Corresponding author at: Department of Physics, Faculty of Science, Universiti Putra Malaysia, UPM, Serdang, Selangor 43400, Malaysia.
E-mail address: saifulasmal@upm.edu.my (M.S.A. Rani).

https://doi.org/10.1016/j.nxnano.2026.100503
Received 1 March 2025; Received in revised form 11 July 2025; Accepted 5 May 2026
Available online 9 May 2026

Table 1
Designation of CE samples.

Composition of $Mg_{0.5+x}(Zr_{1-x}Al_x)_2(PO_4)_3$	Designation
$x = 0$	CE-0
$x = 0.1$	CE-1
$x = 0.2$	CE-2
$x = 0.3$	CE-3
$x = 0.4$	CE-4

for large-scale production but often leads to inhomogeneous products due to limited atomic mixing and requires high calcination temperatures [12,13]. The combustion method provides rapid synthesis and high surface area materials but may result in uncontrolled porosity and incomplete reactions [14]. In contrast, the sol-gel method—particularly the citrate-assisted route—offers better chemical homogeneity at the molecular level, lower synthesis temperatures, and better control over particle size and morphology [15,16]. This makes it especially suitable for preparing complex ceramic systems with precise stoichiometry and improved ionic conductivity. Therefore, in this study, a citric acid-assisted sol-gel method was chosen for synthesizing the target NASICON-type materials due to its advantages in producing high-purity, fine-grained powders with uniform elemental distribution.

In the present work, $Mg_{0.5+x}(Zr_{1-x}Al_x)_2(PO_4)_3$ ($0.0 \leq x \leq 0.4$) compositions were synthesized using the citrate-assisted sol-gel method. To the best of our knowledge, there is no prior report on the use of Al^{3+} substitution in the $Mg_{0.5}Zr_2(PO_4)_3$ structure for enhancing its properties. The structural and electrical properties of the synthesized materials were systematically investigated using X-ray diffraction (XRD), Fourier transform infrared spectroscopy (FTIR), thermogravimetric analysis (TGA), laser particle sizer, field emission scanning electron microscope (FESEM), energy dispersive X-ray (EDX) and impedance spectroscopy (EIS).

2. Experimental

2.1. Materials

All analytical-grade chemical reagents, consisted of magnesium acetate tetrahydrate, zirconium acetate, aluminium acetate, ammonium phosphate, citric acid and acetic acid were employed directly for sol-gel synthesis without any purification.

2.2. Synthesis of $Mg_{0.5+x}(Zr_{1-x}Al_x)_2(PO_4)_3$ ceramic electrolytes

Magnesium acetate tetrahydrate, aluminium acetate and ammonium phosphate were dissolved separately (in specific stoichiometric ratio) with deionised water to initiate hydrolysis reactions. On the other hand, zirconium acetate was dissolved in acetic acid. Citric acid was used to act as chelating agent for the cations with a molar ratio of 1:3 for Cit: Metal. The dissolved reagents were then stirred and mixed together to obtain a homogeneous mixture. The citric acid dissociated upon contact with water and form complex ligands with Mg and Zr. The solution was stirred continuously under magnetic stirring for 24 h on a hot plate at temperature of 75°C under reflux to ensure formation of a homogenous solution. The resulting white gel was dried in an oven at 150°C for 24 h to remove water content and form a precursor powder. The obtained powder was calcined at 400°C (2°C min^{-1}, 6 h) to remove acetate and citrate group. The calcined white powder was then ground to produce discreet particles for the crystallisation process before being sintered at 800 °C for 24 h. The dried powder was then ground again and dry-pressed in a hydraulic uniaxial press at 2 tonnes for 30 s, to form ceramic electrolyte (CE) pellet. The sintered pellet had a final weight of 0.4328 g, with a diameter of 13 mm. The pellet was then reheated at 80 °C for 6 h in air before impedance measurements. Five different sets of CE samples as tabulated in Table 1 were prepared in this work.

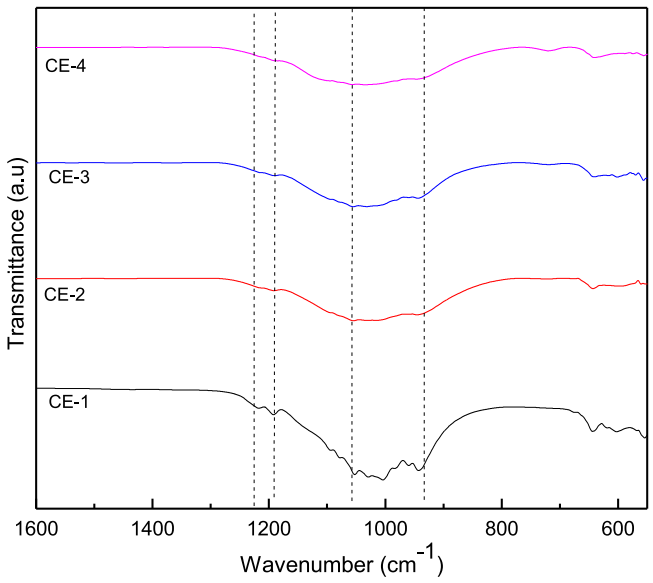

Fig. 1. FTIR spectra of CE samples.

2.3. Characterization techniques

To confirm the structure of the studied compounds, FTIR analysis was carried out using a Perkin Elmer Frontier FTIR spectrophotometer in the range of 1500–700 cm^{-1} with a scanning resolution of 2 cm^{-1}. XRD measurements were taken at room temperature on the compound powders using a PanAlytical X-ray diffractometer equipped with a Cu-Kα radiation source, assembled using Bragg-Brentano configuration. The 2θ range was 18–80° with a step scan of 0.02° per 96 s. The experimental XRD structural data was refined using Rietveld technique employing HighScore Plus 3.0 program and further processed using VESTA program to obtain the Bragg peaks and schematic diagram of the structure. The monoclinic lattice parameters of CEs were calculated using the formula:

$$\frac{1}{d^2} = \frac{1}{\sin^2\beta}\left(\frac{h^2}{a^2} + \frac{k^2\sin^2\beta}{b^2} + \frac{l^2}{c^2} + \frac{2hl\cos\beta}{ac}\right) \quad (1)$$

and

$$d = \frac{\lambda}{2\sin\theta} \quad (2)$$

where d is the distance between crystal planes of (hkl), λ is the X-ray wavelength, θ is the diffraction angle of cystal plane, hkl is the cystal index, a, b, c are the lattice parameters and β is the angle between a and c. The microstructure and elemental composition of final pellets were analysed using FESEM-EDX (Hitachi) with acceleration voltage of 2.0 kV, using cold field emission source. The particle size distribution of CE samples was acquired using FRITSCH-Analysette 22 NanoTec laser particle sizer at ambient temperature. The density (ρ) was determined from sample dimensions and mass using the following equation,

$$\rho = \frac{m}{\pi r^2 t} \quad (3)$$

where m is the sample mass, r is the radius and t is the thickness of the pallete.

Impedance measurements were performed using SOLARTRON 1260 impedance analyser in order to determine the ionic conductivity of the samples. The samples were sandwiched between stainless steel electrodes and measurement was done over the frequency range from 4 MHz to 1 Hz with applied voltage 200 mV. All measurements were done in temperature range 300–500 °C. The total conductivity (σ_t), was

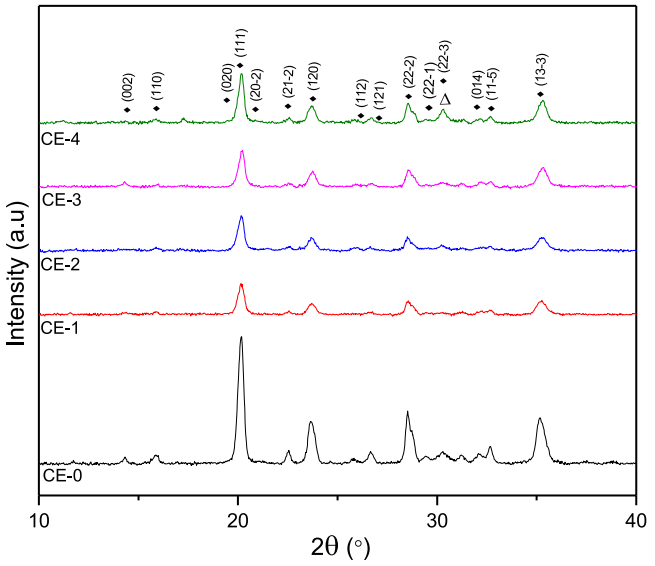

Fig. 2. XRD patterns of CE samples.

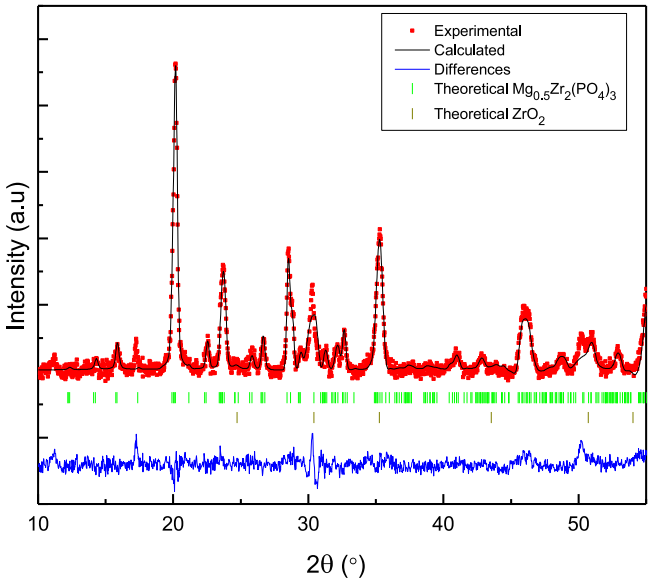

Fig. 3. XRD patterns of CE-4, refined using Rietveld method with $\chi = 1.21$.

calculated using data obtained from the Nquist plot and was evaluated via relation:

$$\frac{1}{\sigma_t} = \frac{1}{\sigma_b} + \frac{1}{\sigma_{gb}} \tag{4}$$

where $\sigma_b = \frac{d}{AR_b}$, $\sigma_{gb} = \frac{d}{AR_{gb}}$, d is the sample thickness, A is the sample-electrode contact area, R_b is the bulk resistance and R_{gb} is the grain boundary resistance. Meanwhile, the AC conductivity was calculated using the equation:

$$\sigma_{ac} = \sigma' = \omega\varepsilon_o\varepsilon'' \tag{5}$$

3. Results and discussions

3.1. FTIR analysis

FTIR spectra of CE samples are depicted in Fig. 1. All four compositions produced the same vibrational and stretching modes; did not produce any considerable change in transmission band positions. The bands in the region of 1280–1020 cm^{-1} are attributed to the υ_3 asymmetric stretching vibrations while those in the region between 980 and 915 cm^{-1} are assigned to υ_4 symmetric stretching vibrations of PO_4^{3-} ions [17,18]. The bands in the region 670–580 cm^{-1} are referred to Zr-O and Zr-O-Zr bonds [19]. These bands intensity decreases with increase of Al^{3+}, which can be explained by the coordination of Al^{3+} with oxygen, leading to the weakening of Zr-O bond. This observation is correlated with the changes of lattice parameters which is explained in the next section.

3.2. Structural study

Shown in Fig. 2 are the XRD patterns of CE samples. All samples can be indexed to monoclinic unit cell with a space group of $P2_{1/n}$ [20]. CE-0 shows sharp and high intensity peaks, however with substitution of Al^{3+} with Zr^{4+}, peaks intensity seems decreasing but the diffraction peaks are still sharp indicating that the produced compounds are in crystalline form. As we can observe from the figure, impurities start to form in the sample CE-4 as indicated by the presence of the peak around 31°. We expected that the impurities would increase if the increase of Al^{3+} content. Thus, analysis was only conducted for the samples with $0.0 \leq x \leq 0.4$.

To study the influences of Al^{3+} substitution in the $Mg_{0.5}Zr_2(PO_4)_3$ crystal lattice, Rietveld refinement was employed as shown in Fig. 3. The enhancement of Mg-ion interstitial was found to influence the structures of CE compounds. The decrease in the unit cell volume with the increase of Al^{3+} can be explained by the existence of additional interstitial Mg^{2+} ion after partial substitution process and the larger atomic size of Al^{3+} than Zn^{4+} in the compounds [21,22]. The density of all compounds decreased after sintering process which is attributed to thermal shrinkage process in citrate sol-gel technique. Besides that, the grain growth process of the compounds also leads to a decrease in crystallite size. As tabulated in Table 2, there are synchronizations between the result of lattice parameters, density and volume of the samples which decrease with the increase of x. The final refined residual factors, R_{wp} and goodness of fitting, GOF (χ^2) for each compositions are also shown in Table 3. As we can see from the Table 3, the low values of R_{wp}, GOF (χ^2) confirms the suitability of the proposed compound structure [23,24].

Fig. 4 shows the schematic diagrams of the CE crystal structure with different plane view and possible impurities in the compounds. However, it can be clearly observed that not all Mg atoms assemble to form a tetrahedral coordination with neighbouring atoms. In Figs. 2 and 3, we can see that peak at ~32° which attributed to a small amount of impurities. Since the purity percentage of CEs is quite high as determined

Table 2
Lattice parameters, unit cell volume and density of CEs palletes.

Samples	a (Å)	b (Å)	c (Å)	V (Å^3)	Density (g cm^{-3})
CE-0	12.427	8.945	8.840	982.65	1.43
CE-1	12.424	8.922	8.827	978.38	1.41
CE-2	12.418	8.918	8.822	976.69	1.37
CE-3	12.416	8.916	8.821	975.89	1.35
CE-4	12.413	8.910	8.820	974.34	1.33

Table 3
R_{wp} and GOF of the CE samples.

Designation	R_{wp}	GOF (χ^2)
CE-0	5.32	0.96
CE-1	4.22	1.25
CE-2	6.13	1.74
CE-3	6.65	1.67
CE-4	4.95	1.21

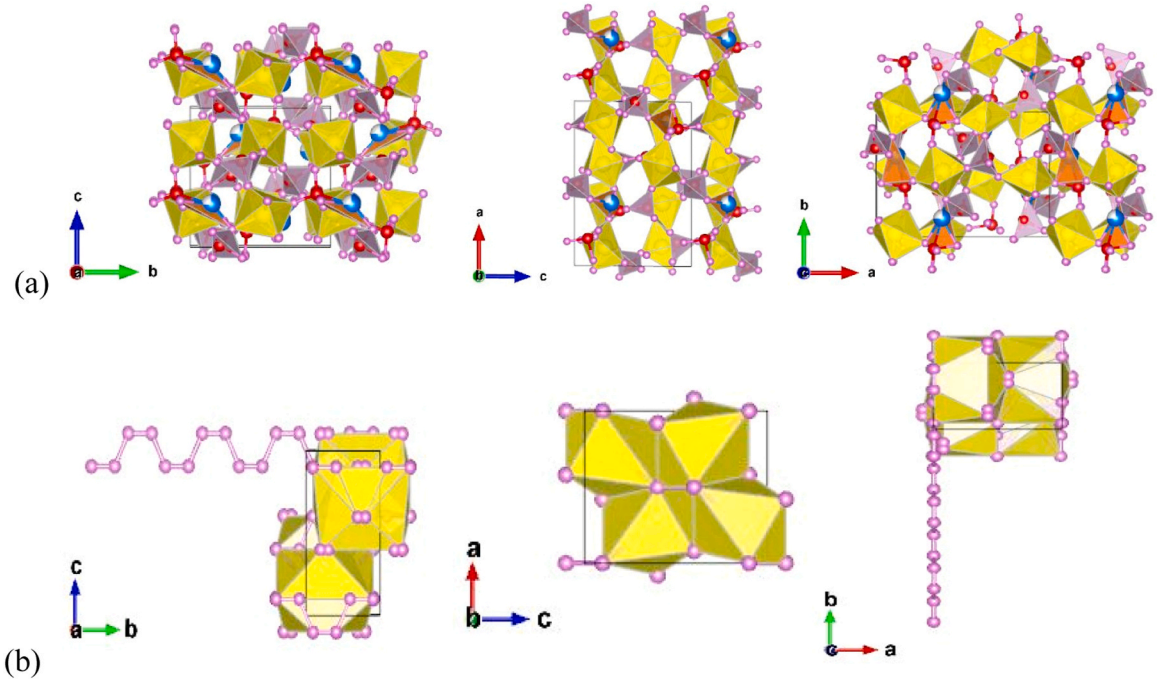

Fig. 4. Schematic diagrams of (a) refined CE crystal structures and (b) possible impurities (Mg: blue; Zr: yellow; P: red; O: pink).

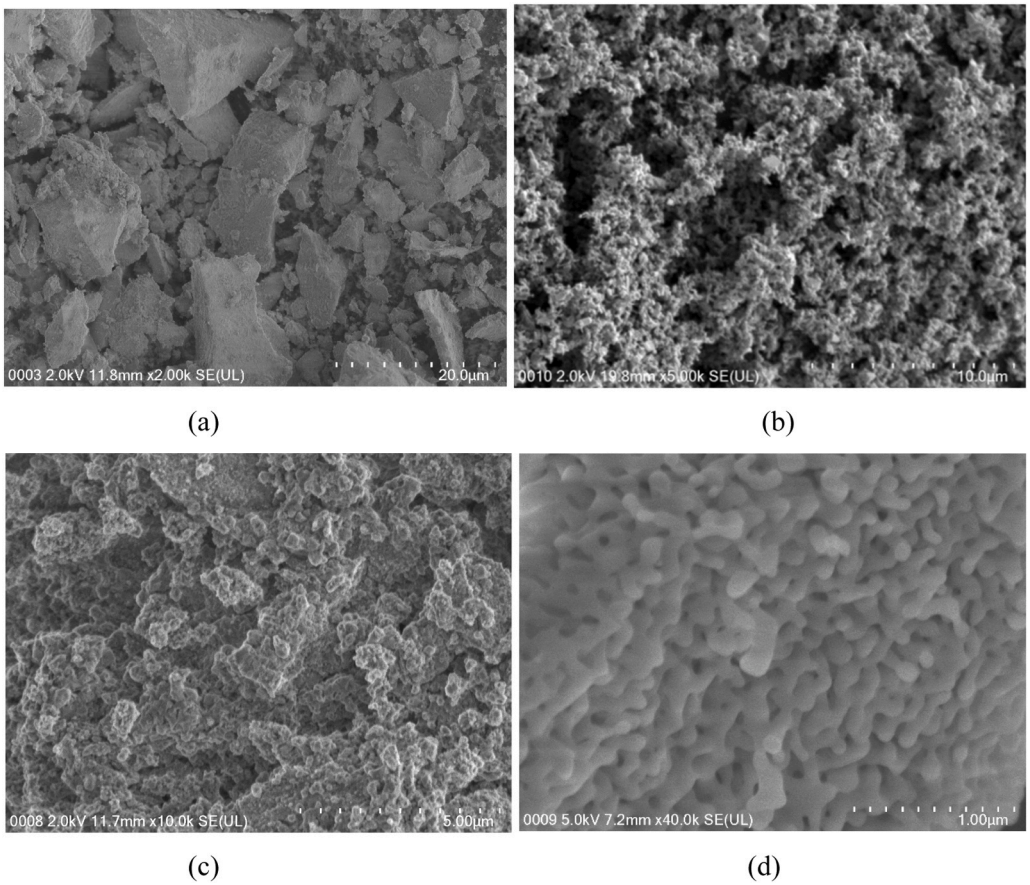

Fig. 5. FESEM micrographs of the CE-4 sample with magnifications of (a) × 2k, (b) × 5k, (c) × 10k and (d) × 40k.

using Rietveld method, the presence of small amount of ZrO_2 (< 4.4%) is expected does not give any significant effects to the electrical and electrochemical properties of the compounds.

3.3. FESEM, EDX and particle size distribution analysis

FESEM micrographs and particle size distributions of CE samples are

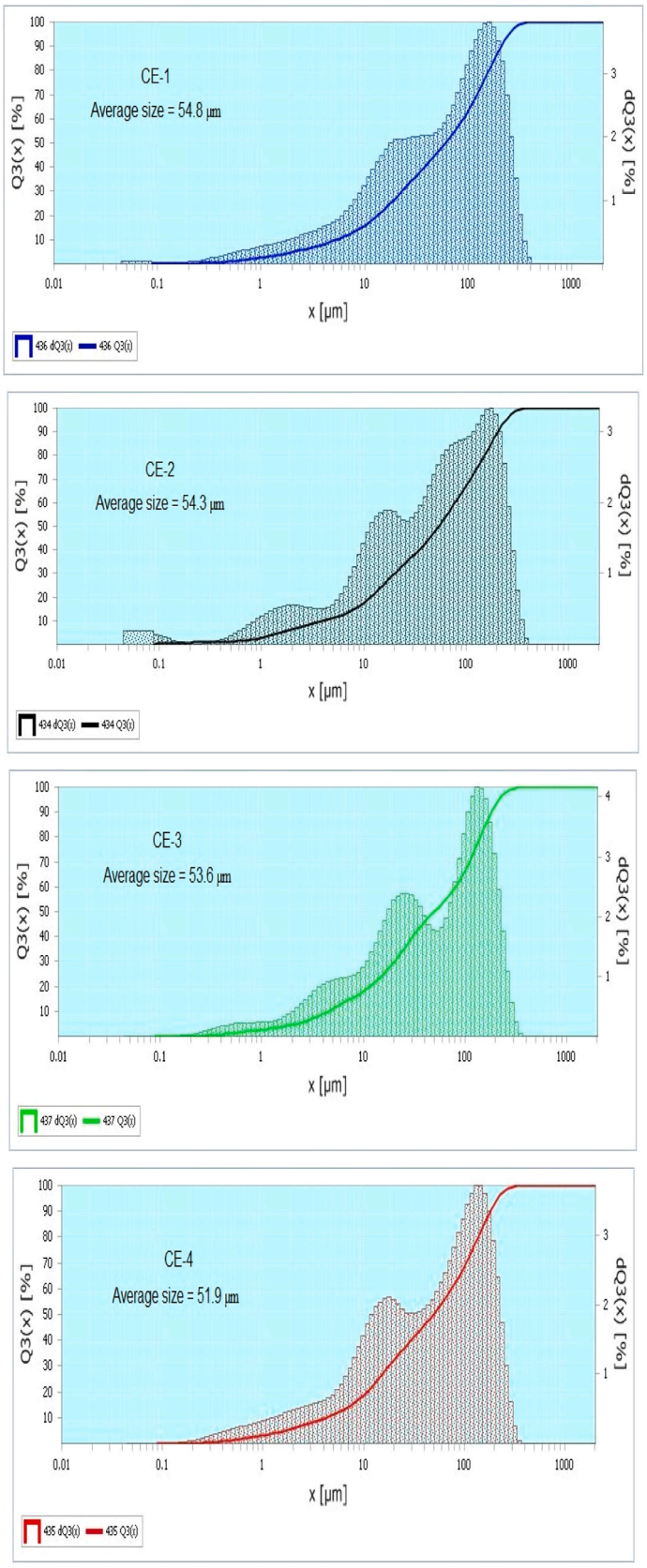

Fig. 6. Particle size distribution of CE compounds.

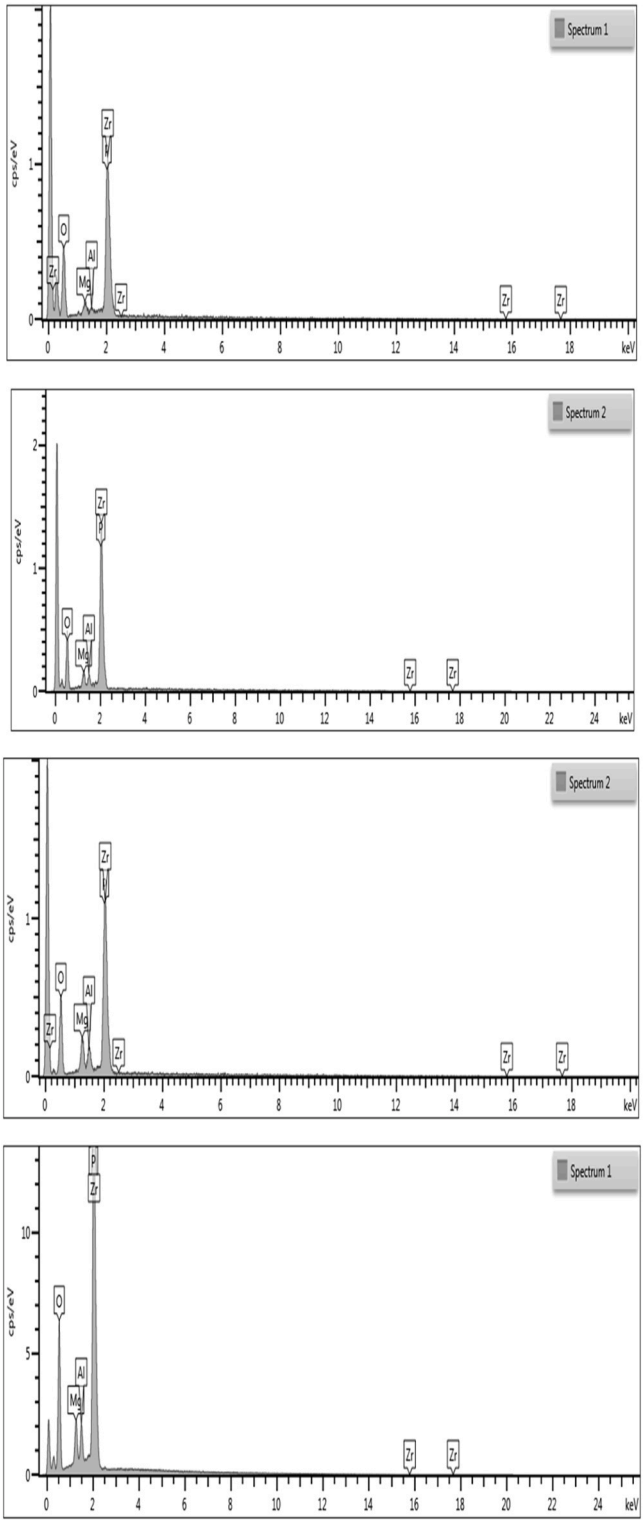

Fig. 7. EDX analysis of CE compounds.

displayed in Fig. 5 and Fig. 6, respectively. The sintering effect can be clearly observed from the figure. The fusing of particles is significant in solid-state electrolyte may lower the resistance attributed to grain boundaries [25]. These results are in agreement with the XRD analysis that shows all samples are in crystalline form. Particle size analysis confirmed that the size reduces with the increase of Al^{3+} in the pure compound. The particle size distribution for CE samples are illustrated in Fig. 6. Fig. 6 clearly illustrates the size of particles in CE samples

Table 4
EDX analysis.

Samples	Composition	Stoichiometric ratio				
		Mg	Zr	Al	P	O
CE-1	Starting mixture (%)	0.6	1.8	0.2	3	12
	EDX analysis (%)	0.62	1.83	0.21	3.1	12.11
CE-2	Starting mixture (%)	0.7	1.6	0.4	3	12
	EDX analysis (%)	0.71	1.58	0.41	3.05	11.96
CE-3	Starting mixture (%)	0.8	1.4	0.6	3	12
	EDX analysis (%)	0.68	1.35	0.59	2.98	12.13
CE-4	Starting mixture (%)	0.9	1.2	0.8	3	12
	EDX analysis (%)	0.9	1.22	0.76	3.1	12.05

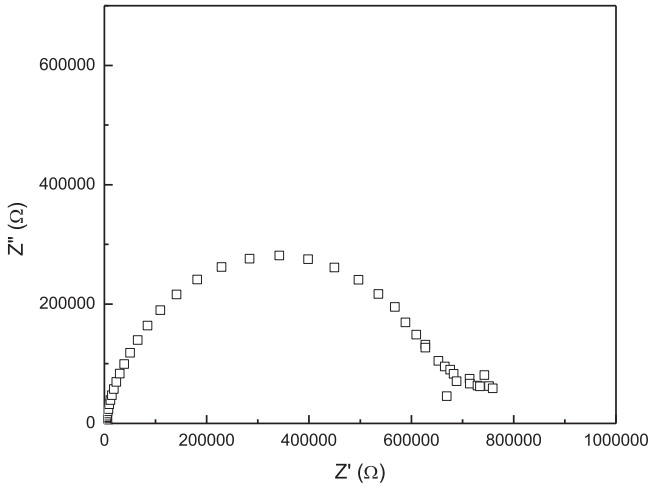

Fig. 8. The impedance spectrum of CE-4 pellet at 673 K.

decreases with the increase of *x*. The particle size decreases from 54.8 μm for CE-0–51.9 μm for CE-4. The smaller particle size would create a large surface area, hence may improve the contact between electrolyte pellete with electrode for electrochemical device applications. EDX spectra of the compounds are displayed in Fig. 7 while analysis for EDX are listed in Table 4. Data analysis for EDX are shown in Table 4 confirms that all compounds not in a good agreement with the stoichiometric formula as designated in CE preparation.

3.4. *Electrical study*

Illustrated in Fig. 8 are typical impedance spectra for CE samples at

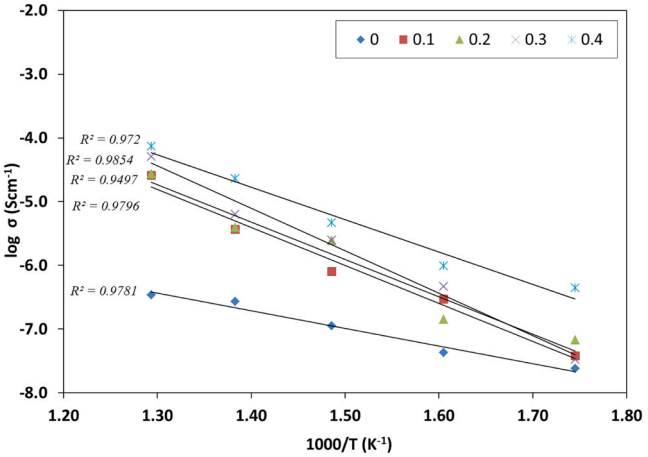

Fig. 9. The temperature dependence of CE compounds.

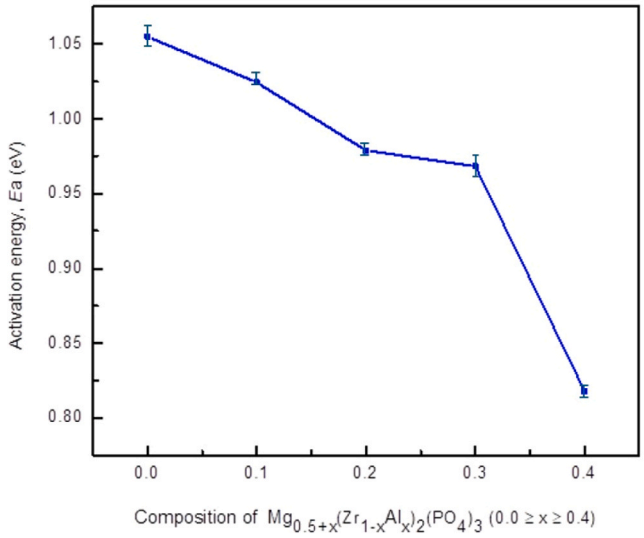

Fig. 10. Activation energy of CE compounds.

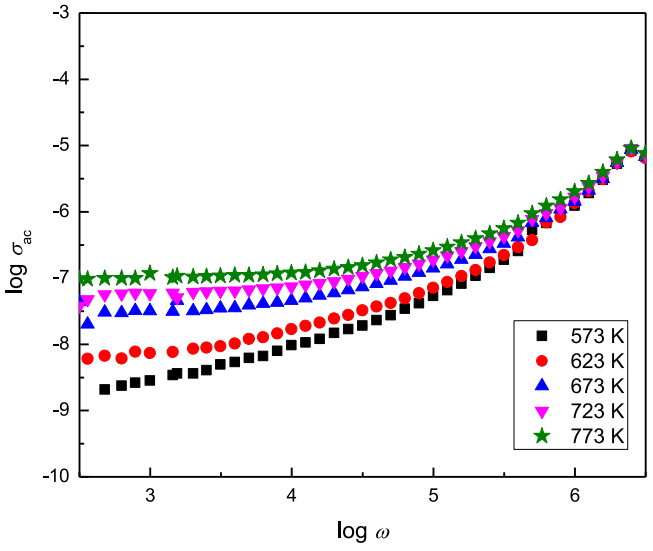

Fig. 11. ac spectra of CE-4.

ambient temperature. The plots consist of two overlapping semicircles with an electrode spike at low frequency region. The semicircle at high frequency is associated with bulk response with the intercept at x-axis (bulk resistance R_b), while grain boundary resistance (R_{gb}) is identified from the middle frequency semicircle with its intercept at the x-axis. This observation is similar with those reported in the literature [26,27]. Electrical investigation were performed on all CE pellets in the temperature ranges from 300 to 500 °C to see the effects of high temperature on their electrical properties. Both R_b and R_{gb} shifted towards lower value as the temperature is increased, indicating an enhancement in conductivity. R_b and R_{gb} values from Nquist plot was used to calculate bulk and grain boundary conductivities (σ_b and σ_{gb}). The total conductivity, σ_t of each sample was calculated using Eq. 6. As Al^{3+} concentration increases, R_t is found to shift towards lower value indicating that the conductivity increases. This can be elaborated by the existence of Mg^{2+} interstitial ions in the lattice structure which leads to enhancement of mobile ions concentration [28,29]. The CE-4 exhibits the highest conductivity of 7.33×10^{-5} S cm^{-1} at 773 K.

Depicted in Fig. 9 is the plot of temperature dependence of conductivity for CE pallets. The conductivity plots of the CE pellets are linear and fit the Arrhenius equation. The thermal activated energy was obtained by using the equation:

$$\sigma_t T = A\exp\left(\frac{-E_a}{kT}\right) \quad (6)$$

where A is the pre-exponential factor, k is the Boltzmann constant and E_a is the activation energy for conduction. As seen in Fig. 9 that all conductivity of all samples increases with the increase in temperature. E_a values were calculated from the slopes of Arrhenius plots depicted in Fig. 10. E_a defined as the energy barrier of an ion to overcome to complete a jump between neighbouring sites [30]. The low E_a values for the CE compounds allowed more species to hop from one site to another which leads to high mobility of ions [31,32]. Lattice contraction also may play an important role in the synthesized compounds. It is noted that the E_a values for the CE compounds decreases with the increase of Al^{3+} concentration. The lowest E_a value, 0.82 EV was obtained for the sample with $x = 0.4$. This result is in good agreement with conductivity results and explains why the highest conductivity value is obtained for this composition.

Presented in Fig. 11 are the log σ_{ac} vs log ω plots for CE samples. These plots are divided into two regions; the low and high frequency regions. The plateau at low frequencies characterizing the DC conductivity is clearly observed. In the high requency region, the transition of direct current plateau to alternate current conductivity dispersion is also observable [33]. As we can see in the figure, σ' increases at the high frequency range. This is according to the universal power law which can be expressed as follows:

$$\sigma'(\omega) = \sigma(0) + A\omega^{\alpha} \quad (7)$$

Where σ(0) is the DC conductivity of the sample, A is a temperature-dependant parameter and α is the power law exponent (represents the degree of interaction between the mobile ion).

4. Conclusion

$Mg_{0.5+x}(Zr_{1-x}Al_x)_2(PO_4)_3$, $(0.0 \le x \le 0.4)$ with high purity percentage was successfully obtained as proven by XRD and Rietveld refinement analysis. Rietveld refinement of XRD measurements on $Mg_{0.5+x}(Zr_{1-x}Al_x)_2(PO_4)_3$ showed optimum phase purity obtained for all compositions. XRD and FTIR analyses confirmed that Al^{3+} was successfully substituted in $Mg_{0.5}Zr_2(PO_4)_3$ structure. $Mg_{0.5+x}(Zr_{1-x}Al_x)_2(PO_4)_3$, $x = 0.4$ or CE-4 exhibited the conductivity of two orders of magnitude higher than the pristine compound. These results reveal that Nasicon-type $Mg_{0.5+x}(Zr_{1-x}Al_x)_2(PO_4)_3$ compound was competence as potential candidates of solid electrolyte in magnesium power storage especially in high temperature device applications.

CRediT authorship contribution statement

M.S.A. Rani: Validation, Investigation, Writing – original draft, Methodology, Writing – review & editing, Project administration. **N.A. Mustaffa:** Software, Validation, Visualization. **Salleh F.:** Funding acquisition, Project administration. **N.S. Mohamed:** Conceptualization, Resources, Supervision. **M. Mustafa:** Methodology, Data curation, Formal analysis.

Declaration of Competing Interest

All authors declare that there is no competing interest.

Acknowledgement

The authors would like to extend their gratitude towards financial support from the Malaysia's Ministry of Higher Education through the Fundamental Research Grant Scheme (Ref. No. FRGS/1/2018/TK07/

UM/01/1).

Data availability

The datasets generated during and/or analysed during the current study are available from the corresponding author on reasonable request.

References

[1] J. Bradley, P. Greene, Solids with high ionic conductivity in group 1 halide systems, Trans. Faraday Soc. 63 (1967) 424–430.
[2] J.B. Goodenough, H.-P. Hong, J. Kafalas, Fast Na+-ion transport in skeleton structures, Mater. Res. Bull. 11 (2) (1976) 203–220.
[3] Guo, N., et al., Stabilizing Zn metal anode through regulation of Zn ion transfer and interfacial behavior with a fast ion conductor protective layer. 2023. **19**(47): p. 2303963.
[4] Wang, T., et al., Stabling zinc metal anode with polydopamine regulation through dual effects of fast desolvation and ion confinement. 2023. **13**(5): p. 2203523.
[5] E. Levi, et al., A review on the problems of the solid state ions diffusion in cathodes for rechargeable Mg batteries, J. Electroceram. 22 (1-3) (2009) 13–19.
[6] Y. Tomita, et al., Li ion conductivity of solid electrolyte, Li3− 2xMxInBr6 (M= Mg, Ca, Sr, Ba), Solid State Ion. 174 (1-4) (2004) 35–39.
[7] K. Makino, et al., Electrochemical insertion of magnesium to Mg0. 5Ti2 (PO4) 3, J. Power Sources 99 (1-2) (2001) 66–69.
[8] K. Makino, et al., Preparation and electrochemical magnesium insertion behaviors of Mg0. 5+ y (MeyTi1− y) 2 (PO4) 3 (Me= Cr, Fe), J. Power Sources 112 (1) (2002) 85–89.
[9] Z. Halim, et al., Effects of Mg2+ interstitial ion on the properties of Mg0. 5+ x/2Si2-xAlx (PO4) 3 ceramic electrolytes, J. Magnes. Alloy. 5 (4) (2017) 439–447.
[10] S.S.J.J. Zhang, A review on the separators of liquid electrolyte Li-ion batteries 164 (1) (2007) 351–364.
[11] Cassel, A., et al., Sol-gel synthesis and electrochemical properties extracted by phase inflection detection method of NASICON-type solid electrolytes LiZr2 (PO4) 3 and Li1. 2Zr1. 9Ca0. 1 (PO4) 3. 2017. 309: p. 63-70.
[12] A. Kumar, et al., Solid-state reaction synthesis of nanoscale materials: strategies and applications 122 (15) (2022) 12748–12863.
[13] J. Li, et al., Recent advances in the large-scale production of photo/electrocatalysts for energy conversion and beyond 14 (45) (2024) 2402441.
[14] E. Novitskaya, et al., A review of solution combustion synthesis: an analysis of parameters controlling powder characteristics 66 (3) (2021) 188–214.
[15] C. Suryanarayana, N.J. Al-Aqeeli, Mechanically alloyed nanocomposites, Progress Mater. Sci. 58 (4) (2013) 383–502.
[16] S. Arya, et al., Influence of processing parameters to control morphology and optical properties of Sol-Gel synthesized ZnO nanoparticles 10 (2) (2021) 023002.
[17] A. Bohre, O. Shrivastava, Crystal chemistry of immobilization of divalent Sr in ceramic matrix of sodium zirconium phosphates, J. Nucl. Mater. 433 (1-3) (2013) 486–493.
[18] E.Y. Borovikova, et al., Infrared spectroscopy and the structure of La 0.33 Zr 2 (PO 4) 3-Yb 0.33 Zr 2 (PO 4) 3 solid solutions, J. Struct. Chem. 51 (1) (2010) 40–44.
[19] F. Ejehi, et al., The synthesis of NaSICON-type ZrNb (PO4) 3 structure by the use of Pechini method, Ceram. Int. 38 (8) (2012) 6857–6863.
[20] E. Gobechiya, et al., Crystal structure of the double magnesium zirconium orthophosphate at temperatures of 298 and 1023 K, Crystallogr. Rep. 53 (1) (2008) 53–59.
[21] P.G. Bruce, J. Evans, C.A. Vincent, Conductivity and transference number measurements on polymer electrolytes, Solid State Ion. 28 (1988) 918–922.
[22] M. Riley, P.S. Fedkiw, S.A. Khan, Transport properties of lithium hectorite-based composite electrolytes, J. Electrochem. Soc. 149 (6) (2002) A667–A674.
[23] T. Pareek, et al., LiSnZr (PO4) 3: NASICON-type solid electrolyte with excellent room temperature Li+ conductivity, J. Alloy. Compd. 777 (2019) 602–611.
[24] X. Zhang, et al., Structure, site-occpancy and luminescent properties of a novel blue phosphor Na3ZrMgP3O12: Eu2+, Mater. Res. Bull. 106 (2018) 396–402.
[25] N. Johari, et al., Structural and electrical properties of Na2ZnSiO4-Py14TFSI hybrid solid electrolyte, Ceram. Int. (2019).
[26] X. Xu, et al., The preparation and lithium mobility of zinc based NASICON-type solid electrolyte Li1+ 2x+ 2yAlxZnyTi2− x− ySixP3− xO12, Ceram. Int. 40 (2) (2014) 3819–3822.
[27] M. Mustafa, et al., Characteristics of new Mg0. 5 (Zr1-xSnx) 2 (PO4) 3 NASICON structured compound as solid electrolytes, Ceram. Int. 46 (18) (2020) 28145–28155.
[28] K. Nomura, et al., Framework structure, phase transition and ionic conductivity of MgZr4 (PO4) 6 and ZnZr4 (PO4) 6, J. Electroanal. Chem. 326 (1-2) (1992) 351–356.
[29] H. Takahashia, H. Takamura, Ionic conductivity and crystal structure of TM-doped Mg0. 5Ti2 (PO4) 3 (TM= Fe, Mn, Co and Nb). Key Eng. Mater., Trans Tech Publ, 2012.
[30] M. Rani, et al., Conductivity and dielectric behavior studies of carboxymethyl cellulose from kenaf bast fiber incorporated with ammonium acetate-BMATFSI biopolymer electrolytes, Int. J. Polym. Anal. Charact. 20 (3) (2015) 250–260.
[31] M.S.A. Rani, A. Ahmad, N.S. Mohamed, A comprehensive investigation on electrical characterization and ionic transport properties of cellulose derivative from kenaf fibre-based biopolymer electrolytes, Polym. Bull. 75 (11) (2018) 5061–5074.
[32] N.S.M. Johari, et al., High-throughput development of Na2ZnSiO4-based hybrid electrolytes for sodium-ion batteries, J. Power Sources 541 (2022) 231706.
[33] Z. Halim, S. Adnan, N. Mohamed, Effect of sintering temperature on the structural, electrical and electrochemical properties of novel Mg0. 5Si2 (PO4) 3 ceramic electrolytes, Ceram. Int. 42 (3) (2016) 4452–4461.